catalysts

MDPI

Article

Surface-Subsurface Preference of S Species on Transition Metal Nanoparticles: A DFT Study

Iskra Z. Koleva [1,*], Ivana Hristova [1], Boyana Sabcheva [1], Polya V. Koleva [1], Francesc Viñes [2,*] and Hristiyan A. Aleksandrov [1,*]

[1] Faculty of Chemistry and Pharmacy, Sofia University "St. Kliment Ohridski", 1164 Sofia, Bulgaria
[2] Departament de Ciència de Materials i Química Física & Institut de Química Teòrica i Computacional (IQTCUB), Universitat de Barcelona, c/Martí i Franquès 1, 08028 Barcelona, Spain
* Correspondence: ohik@chem.uni-sofia.bg (I.Z.K.); francesc.vines@ub.edu (F.V.); haa@chem.uni-sofia.bg (H.A.A.)

Abstract

Sulfur is a well-known catalyst poison, particularly for catalysts based on transition metals. Herein, we studied the adsorption of sulfur species on small nanoparticles (~1 nm in size) of the face centered cubic (fcc) transition metals (Rh, Ir, Ni, Pd, Pt, Cu, Ag, and Au) using density functional theory (DFT) modeling. At low sulfur coverage (one S atom per nanoparticle), sulfur preferentially occupies the surface hollow sites of the nanoparticles. At higher coverage, however, the subsurface diffusion of S in Ni, Pd, and Ag nanoparticles becomes energetically favorable with low activation energies. Among the considered metals, sulfur binds most strongly to Rh and Ir, and most weakly to Ag and Au. The present results shed light on the facility of S-poisoning on such metal nanoparticles, either by surface blocking or by underlying sulfurization of the metal.

Keywords: transition metals; sulfur adsorption; subsurface diffusion; DFT; nanoparticles

1. Introduction

Sulfur (S) plays a complex role in heterogeneous catalysis involving transition metals. As an omnipresent impurity in fossil fuels and many industrial reactions, sulfur is well-known for its strong affinity for metal surfaces on which it can adsorb, block the active sites and modify the electronic properties of the catalyst. These effects usually lead to catalyst deactivation—the so-called poisoning, often observed in industrially important processes such as reforming, methanation, Fischer–Tropsch synthesis, fuel cell power production, hydroprocessing and oxidation [1]. This makes sulfur tolerance a key challenge in catalyst design. Sulfur usually originates from species such as H_2S, SO_2, SO_4^{2-}; as in this order, the toxicity for poisoning a given metal decreases due to increasing oxygen shielding of the sulfur atom [1]. The mechanism of poisoning could be divided into four main components: (i) the sulfur atom strongly adsorbs to the metal surface and thus blocks at three- or four-fold reaction/catalytic sites; (ii) the electronic properties of the metal atoms bound to the sulfur and in some cases the next nearest neighbor atoms are modified due the strong chemical binding, thus changing their capacity to adsorb and/or dissociate reactant molecules such as H_2 and ethylene; (iii) the strong adsorption also often leads to surface relaxation, which can significantly change/alter the catalytic properties; (iv) the adsorbed S blocks the access of the adsorbed reactant molecules to each other and also hinders their surface diffusion [1]. For example, even trace levels of H_2S (2–10 ppm) dramatically

Check for updates

Academic Editors: Salah-Eddine Stiriba and Ning Liu

Received: 14 January 2026
Revised: 11 March 2026
Accepted: 19 March 2026
Published: 1 May 2026

Copyright: © 2026 by the authors. Licensee MDPI, Basel, Switzerland. This article is an open access article distributed under the terms and conditions of the Creative Commons Attribution (CC BY) license.

decrease the activity of Ni/Al_2O_3 and Ni/CeO_2 catalysts in steam methane reforming reaction due to the sulfidation and cannot be fully recovered even when the H_2S is removed from the feed [2].

Pt and Pd, usually supported on alumina, are widely used for CO oxidation due to their high catalytic activity [3–5]. However, a major drawback of these catalysts is their propensity towards sulfur poisoning in sulfur-rich exhaust gases [6–8]. The sulfur tolerance of platinum can be enhanced by using TiO_2 support [9]. It was shown that Pt/TiO_2 catalyst is more resistant to sulfur poisoning due to the spillover of sulfur species from Pt to TiO_2.

However, interestingly, in some cases, sulfur, by altering the strong adsorption (binding strength), may tune the catalyst properties. For example, it was found that in a sulfur-doped Mo_2C catalyst with high activity and stability toward electrochemical hydrogen under acidic reaction conditions, sulfur acts as a promoter by weakening the hydrogen binding energy, which is generally considered to bind hydrogen too strongly [10]. In another study, it was shown that S species can hinder the catalytic activity of Rh nanoparticles towards methanol carbonylation but surprisingly promote the monoatomic Rh species in this reaction [11]. Sulfur also may influence the selectivity of the catalysts by changing the preferred reaction path, e.g., to hinder unwanted side reactions and promote the desirable ones. It was shown by density functional theory (DFT) modeling of the Fischer–Tropsch (FT) reaction on Co(111) surfaces that S decreases the adsorption energies of CO, HCO and ethyne species and alters selectivity via changes in the activation barriers—lowering those for carbon and oxygen hydrogenation and increasing those for CO dissociation and CH coupling [12]. In addition, sulfur can adjust metal-metal or metal-ligand distances, changing active site geometry. For example, in the case of Mn-based catalyst (Mn-N-C-S) for oxygen reduction reaction, the high-shell sulfur doping strengthened the Mn–N bonds and increased spin density of Mn sites [13]. In the CO_2 methanation reaction catalyzed by Ru/Al_2O_3, the increase of sulfur content was found to cause a gradual decrease in CO_2 conversion, accompanied by an increase in CO selectivity [14]. The formation of Ru sulfides on the catalyst surface was observed, leading to a reduced adsorption capacity for both H_2 and CO in the sulfur-poisoned samples. In addition, the electronic effect of sulfur weakens the Ru–CO bond, resulting in a lower CO desorption temperature.

The adsorption of sulfur on (111) surfaces of Rh [15,16], Ir [14,17], Ni [14,18–20], Pd [14,21], Pt [14,22], Cu [14,20,23,24], Ag [14,20,25], Au [14,26,27] transition metals was already computationally studied and the preferred adsorption sites and the binding energy of sulfur have been reported. Other surfaces such as M(100), (110), and (211) (M = Rh, Ir, Ni, Pd, Pt, Cu, Ag, Au) [14,26,28] were also extensively investigated. However, the nanoparticle models are more realistic from an experimental point of view, since they provide low-coordinated sites at their edges and corners, which offer stronger binding to adsorbates and greater flexibility. In this study, we employed DFT calculations to investigate the interaction of S with all the *fcc* metals. At variance with previous studies, we employed Rh_{79}, Ir_{79}, Ni_{79}, Pd_{79}, Pt_{79}, Cu_{79}, Ag_{79} and Au_{79} nanoparticle models to examine not only regular hollow and bridge sites but also sites including low-coordinated metal centers close to the edges and corners of the models. For this aim all possible surface/subsurface ad/absorption sites on/beneath (111) facets of the nanoparticles were investigated. To the best of our knowledge, this is the first systematic study addressing the effect of sulfur coverage on its binding energy, and its subsurface diffusion was considered by models containing a larger amount of sulfur. In addition, various electronic characteristics (d-band center, Bader charges, electronegativity, etc.) of transition metal nanoparticles and S species adsorbed on them were also considered. To our knowledge, in our work for the first time, the occupation of d-orbitals with electron density is considered and found to be an important descriptor for the binding strength of S. The two contributions to the

binding energy of the S species—interaction energy and relaxation energy of the transition metal nanoparticles—were analyzed. A comparison of the S behavior on extended and nanoparticle models was also performed.

2. Results

The generalized model of the metal nanoparticles is shown in Figure 1. The nanoparticle (NP) shape was chosen as a truncated octahedron, given that it is the Wulff construction shape that minimizes the overall nanoparticle surface tension [29] and is regularly at the onset of being in the scalable regime, its sites being representative of larger nanoparticles [30]. The four non-equivalent surface hollow positions are denoted as *fcc-cen*, *fcc-cor*, *hcp-cor*, and *hcp-edg*. The corresponding tetrahedral and octahedral subsurface positions below them are correspondingly named *oss-cen*, *oss-cor*, *tss-cor,* and *tss-edg*. We also modeled the tetrahedral position, denoted as *tss'*, which is located beneath a surface metal atom at the center of the (111) facet (*cen* site). The coordination number (CN) of the atoms located in the middle of the (111) facets (*cen* sites) is nine (six surface and three subsurface metal atoms). Atoms on the edges and corners of the facets (called *edg* and *cor* sites) are with lower CN—seven and six, respectively, as in both cases the metal center is bound to one subsurface atom.

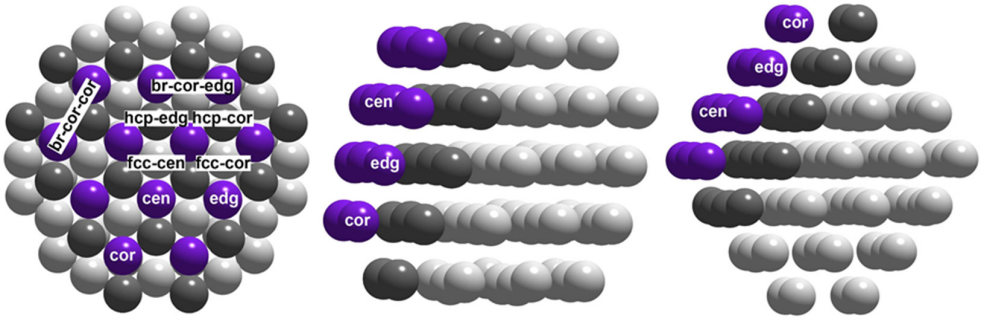


Figure 1. Top and side views of the studied surface and subsurface positions of S on M_{79} NP. For visual clarity, the atoms belonging to one of the (111) facets are colored in purple and those of the first subsurface layer below this facet in dark gray. The notation of the surface metal atoms with different coordination numbers (**all panels**), as well as the adsorption hollow and bridge sites (**left panel**), is also presented.

2.1. Interaction with One Sulfur Atom

The interaction of a single sulfur atom with the *fcc* transition metal nanoparticles studied in this work reveals a strong preference of S for adsorption on the nanoparticle surface. Among all examined adsorption sites, the *fcc-cor* position emerges as one of the most energetically favorable across the series of studied metals (see Tables S1–S3 in Supplementary Materials). This configuration is particularly advantageous for the Ni_{79}, Cu_{79}, Ag_{79}, and Au_{79} structures, while for the remaining S/M_{79} systems, the binding energies associated with their most stable configurations are comparable to those at the *fcc-cor* site. For group 9 metals, the *hcp-cor* position provides the strongest stabilization, with binding energies of −533 kJ/mol and −529 kJ/mol for Rh_{79} and Ir_{79}, respectively (see Table S1), as in both cases, very close in stability is *fcc-cor* position. For group 10 metals, the sulfur atom binds most strongly at both *fcc-cen* and *fcc-cor* positions. The binding energies collaborate within 1, 1, and 8 kJ/mol for both positions at Ni, Pd, and Pt, respectively, as the corresponding values for the most stable position are −502, −487, and −516 kJ/mol, respectively (cf. Table S2). For the Ni_{79} nanoparticle, a third position, *hcp-cor*, is close in energy (4 kJ/mol difference) to the most stable *fcc-cor*. Among all metal systems studied, the strongest sulfur-surface interactions are observed for the Rh_{79} and Ir_{79} nanoparticles, with binding energies ranging from −517 to −533 kJ/mol and −497 to −529

kJ/mol, respectively (see Table S1). On the contrary, the weakest interactions are observed for the Au_{79} and Ag_{79} systems, with corresponding binding energies in the range of −363 to −386 kJ/mol and −354 to −370 kJ/mol, respectively (see Table S3).

When sulfur is initially placed in octahedral or tetrahedral subsurface environments, geometry optimization typically results in migration to surface *fcc* or *hcp* sites for all NPs. In most cases, we were able to achieve structures with subsurface S species only when they are positioned at the octahedral position beneath the center of a (111) facet. Such *oss-cen* configurations were obtained for six of the nanoparticles—Rh_{79}, Ir_{79}, Ni_{79}, Pd_{79}, Pt_{79} and Ag_{79}. This subsurface coordination induces structural deformation in the (111) facets of Rh_{79}, Ir_{79}, Ni_{79} and Ag_{79}, as the three surface-layer metal atoms directly bonded to S are displaced above the surface level. In such configurations, the sulfur atom remains closer to the low-coordinated metal surface atoms than to the underlying subsurface region. A comparison of the binding energies at the center of the facet reveals that surface adsorption of S is significantly more favorable than subsurface positions, with energy differences ranging from 91 to 409 kJ/mol. The largest one is observed for the Ir_{79} NP, while the smallest occurs in the Ag_{79} structures. Furthermore, no stable subsurface positions were identified for the Cu_{79} nanoparticles, indicating a strong tendency for sulfur to favor surface coordination in this system. When sulfur is positioned in the *tss*′ position, this leads to structural reconstruction in half of the metals studied during the geometry optimization. In the S/Ag_{79} complex, S migrates to the level of the surface silver atoms, displacing one Ag atom upward. A comparable reconstruction is observed in the S/Pd_{79} complex, where sulfur remains in a subsurface position but is located closer to the surface layer. In the case of Au_{79}, the heteroatom shifts toward the second metal layer. In contrast, for Rh_{79}, Ir_{79}, Ni_{79}, and Cu_{79}, sulfur spontaneously migrates from *tss*′ to a surface site during optimization. When S is positioned in a subsurface position different from *oss-cen*, it either emerges on the surface or makes subsurface reconstructions. These reconstructed subsurface structures are usually less stable than the corresponding *oss-cen* structure. The only exception is Au_{79}, where the reconstructed Au-S-tss′ is the optimized structure with subsurface S.

Bridge configurations (*br_cor-cor*, *br_cor-edg*, *br_cor-cen*, *br_edg-cen*, *br_cen-cen*) were also examined for the M_{79}/S systems. However, for all metal nanoparticles, the sulfur atom in the latter three coordination types spontaneously relocates to hollow sites during geometry optimization. Only, in the case of Ir_{79} NP, *br_cor-edg* and *br_cor-cor* positions are close in stability by ~10 kJ/mol to the most favorable hollow sites–*hcp-cor* and *fcc-cor*. For Rh_{79}, Ni_{79}, Pd_{79}, Pt_{79} and Au_{79} NPs, those configurations are by 35–80 kJ/mol less favorable than the corresponding most stable structures with hollow S coordination. For Cu_{79} and Ag_{79} nanoparticles, S species in *br_cor-edg* and *br_cor-cor* positions move to hollow ones during the optimization procedure.

2.2. High S Surface Coverage

To examine the potential for subsurface sulfur diffusion at higher surface coverage, for each metal nanoparticle, structures saturated with four—$^1/_3$ of a monolayer (ML) coverage per (111) facet—and seven—$^7/_{12}$, i.e., 58% of a ML coverage per (111) facet—S atoms were constructed. In both cases, two types of configurations were considered: in the first one, all sulfur atoms are located in the *fcc* hollow sites on the (111) facet; in the second one, the S atom at the center of the facet (*fcc-cen*) was placed in the corresponding subsurface octahedral position (*oss-cen*). By comparing the energies of both types of structures, we can conclude that in most cases, S prefers to occupy the *fcc-cen* position instead of sinking into the subsurface layer of the NPs (see Table 1). The subsurface position is most disfavored in the case of Ir_{79} NP for both models with four (Ir-3S-fcc-1S-*oss-cen*) and seven (Ir-6S-*fcc*-1S-*oss-cen*) S atoms, as they are unstable by 248 and 147 kJ/mol, respectively, compared

to the corresponding structures possessing surface S atoms only (Ir-4S-*fcc* and Ir-7S-*fcc*). At sulfur coverage of $^{1}/_{3}$ ML, the subsurface sinking of S is favorable only in the case of Ag NP, albeit with a modest stabilization of 12 kJ/mol. Upon further increase in S to 58% or $^{7}/_{12}$ of a ML, the subsurface diffusion also becomes favorable for Ni and Pd NPs, as such structures are more stable by 35 and 42 kJ, respectively, compared to the models with surface sulfur. It should be noted that, in the case of Ag_{79}, a strong relaxation of the surface layer of the NP occurs, and in the Ag-7S-fcc structure, during the optimization, the S atom initially located in *fcc-cen* site migrates spontaneously to the corresponding subsurface position—*oss-cen*. In the Ag-6S-fcc-1S-oss-cen model, a significant relaxation of the (111) facet on which sulfur atoms are adsorbed is also observed. Thus, the obtained models (Ag-7S-*fcc* and Ag-6S-*fcc*-1S-*oss-cen*) are practically the same in geometry. This implies that upon higher sulfur coverage, the S species spontaneously penetrates into the subsurface layer of the Ag_{79} NP. In the case of Cu, the Cu-6S-*fcc*-1S-*oss-cen* model is disfavored by only 14 kJ/mol compared to the corresponding model with all surface S species, Cu-7S-*fcc*. For Cu, Ag and Au (structures Cu-4S-*fcc*, Ag-4S-*fcc* and Au-4S-*fcc*), the S atom initially located at the *fcc-cen* site, during the optimization, moves very close to the level of the metal surface atoms. Similarly, in Cu-7S-*fcc* and Au-7S-*fcc* models, the S species are at the level of the surface metal centers.

Table 1. Relative energies, ΔE in kJ/mol, with respect to the most energetically stable structure in the series, binding energy of the sulfur atom, BE in kJ/mol, and activation energies for the subsurface diffusion process (*fcc-cen* → *oss-cen*), E_a in kJ/mol.

Structure	ΔE	BE [a]	BE(*fcc-cen*/*oss-cen*) [b]	E_a
Rh-4S-*fcc*	0	−494	−397	
Rh-3S-*fcc*-1S-*oss-cen*	128	−462	−269	
Rh-7S-*fcc*	0	−479	−441	
Rh-6S-*fcc*-1S-*oss-cen*	56	−471	−385	
Ir-4S-*fcc*	0	−490	−390	
Ir-3S-*fcc*-1S-*oss-cen*	248	−428	−142	
Ir-7S-*fcc*	0	−478	−428	
Ir-6S-*fcc*-1S-*oss-cen*	147	−457	−281	
Ni-4S-*fcc*	0	−463	−351	
Ni-3S-*fcc*-1S-*oss-cen*	88	−441	−263	
Ni-7S-*fcc*	35	−445	−383	
Ni-6S-*fcc*-1S-*oss-cen*	0	−450	−418	23
Pd-4S-*fcc*	0	−451	−363	
Pd-3S-*fcc*-1S-*oss-cen*	60	−436	−303	
Pd-7S-*fcc*	42	−425	−300	
Pd-6S-*fcc*-1S-*oss-cen*	0	−431	−342	57
Pt-4S-*fcc*	0	−482	−408	
Pt-3S-*fcc*-1S-*oss-cen*	140	−447	−268	
Pt-7S-*fcc*	0	−465	−373	
Pt-6S-*fcc*-1S-*oss-cen*	56	−457	−317	
Cu-4S-*fcc*	0	−417	−334	
Cu-3S-*fcc*-1S-*oss-cen*	32	−409	−302	
Cu-7S-*fcc*	0	−389	−322	
Cu-6S-*fcc*-1S-*oss-cen*	14	−387	−308	17/3 [d]
Ag-4S-*fcc*	12	−346	−275	
Ag-3S-*fcc*-1S-*oss-cen*	0	−349	−287	2
Ag-7S-*fcc* [c]		becomes Ag-6S-fcc-S-oss-cen		
Ag-6S-*fcc*-1S-*oss-cen* [c]		−360	−322	

Table 1. *Cont.*

Structure	ΔE	BE [a]	BE(*fcc-cen*/*oss-cen*) [b]	E_a
Au-4S-*fcc*	0	−380	−401	
Au-3S-*fcc*-1S-*oss-cen*	192	−332	−209	
Au-7S-*fcc*	0	−340	−277	
Au-6S-*fcc*-1S-*oss-cen*	140	−320	−137	

[a] per one S atom; [b] BE of the S at *fcc-cen* or *oss-cen* position; [c] both structures have very similar geometry since a significant reconstruction of the (111) facet, where S is adsorbed, is observed; [d] 3 kJ/mol is the barrier for emerging on the surface.

For all of the NPs, the increase in the sulfur concentration leads to a decrease in the energetic difference between the configuration with surface S species only and the corresponding ones containing one subsurface S. For example, for Rh_{79} NP, when only one S is adsorbed at *fcc-cen* position—$^1/_{12}$ of a ML or 8% S coverage per (111) facet—, the corresponding subsurface position (*oss-cen*) is less stable by 250 kJ/mol (see Table S1). At the higher S concentrations −33 and 58%, the instability of the *oss-cen* site is reduced to 128 and 56 kJ/mol, respectively (cf. Table 1).

As in the case of the models with one S atom, the strongest surface binding of sulfur species is observed for the metal nanoparticles of group 9, with average binding energies of −494 (4 S atoms) and −479 kJ/mol (7S atoms) for Rh_{79} and −490 and −478 kJ/mol for Ir_{79}. The weakest binding is found in the Ag_{79} and Au_{79} systems, −340 ÷ −380 kJ/mol. A similar trend is observed in the configurations with four/six S surface atoms and one S subsurface atom: Rh_{79} again exhibits the most favorable binding (−462/−471 kJ/mol), while Au_{79} shows the least favorable interaction (−332/−320 kJ/mol). The individual binding energies of the S species at the *fcc-cen* and *oss-cen* positions were also calculated. In all cases, except for Au-4S-*fcc*, they are lower in absolute value compared to the average binding energy per S atom.

Since sulfur diffusion in the subsurface layer is energetically favorable (exothermic) for Ni, Pd, and Ag nanoparticles at the highest considered S coverage of 58%, the activation energies for this process were calculated (see Table 1 and Figure 2). The resulting energy barriers are 23, 57, and 2 kJ/mol, respectively, indicating that the diffusion process is also kinetically feasible. Even the highest barrier calculated in the case of Pd is expected to be readily overcome under catalyst operating conditions, whereas for the Ag NP, the sinking of S is essentially barrierless. For the Cu nanoparticle, although the subsurface diffusion is energetically slightly unfavorable by 14 kJ/mol, the barrier for sulfur sinking was also evaluated and found to be only 17 kJ/mol. This result implies that the reverse process—sulfur emerging on the surface—would have an activation barrier of only 3 kJ/mol.

2.3. Electronic Properties

In most cases, partial electron transfer from the neighboring metal centers to the sulfur atom is observed, as this effect is most pronounced when S is adsorbed on Ag_{79} and Cu_{79} NPs (see Table 2). The sulfur Bader charge at *fcc-cen* position is almost neutral, −0.02 |e|, for S/Pt_{79} and slightly more negative, from −0.15 to −0.23 |e|, for S/Pd_{79}, S/Ir_{79}, S/Au_{79}, and S/Rh_{79}. The highest negative values were calculated for S/Ni_{79}, S/Ag_{79}, and S/Cu_{79}, −0.44, −0.57 and −0.60 |e|, respectively. For the *oss-cen* position the values remain the same for the metals with lowest values, S/Ni_{79} and S/Ag_{79}, while for the other metals the negative values decrease in magnitude by 0.11–0.17 |e|, as they become essentially neutral for S/Pd_{79} and S/Ir_{79}, while in the case of S/Pt_{79} system, the sulfur is even slightly positively charged, 0.13 |e|. This decrease in the negative charge of S when positioned subsurface can be rationalized by the formation of more metal-S contacts. As the S species

possesses two lone pairs, it can participate in donor–acceptor type interactions with the metal centers, which have empty frontier orbitals with appropriate symmetry and energy.

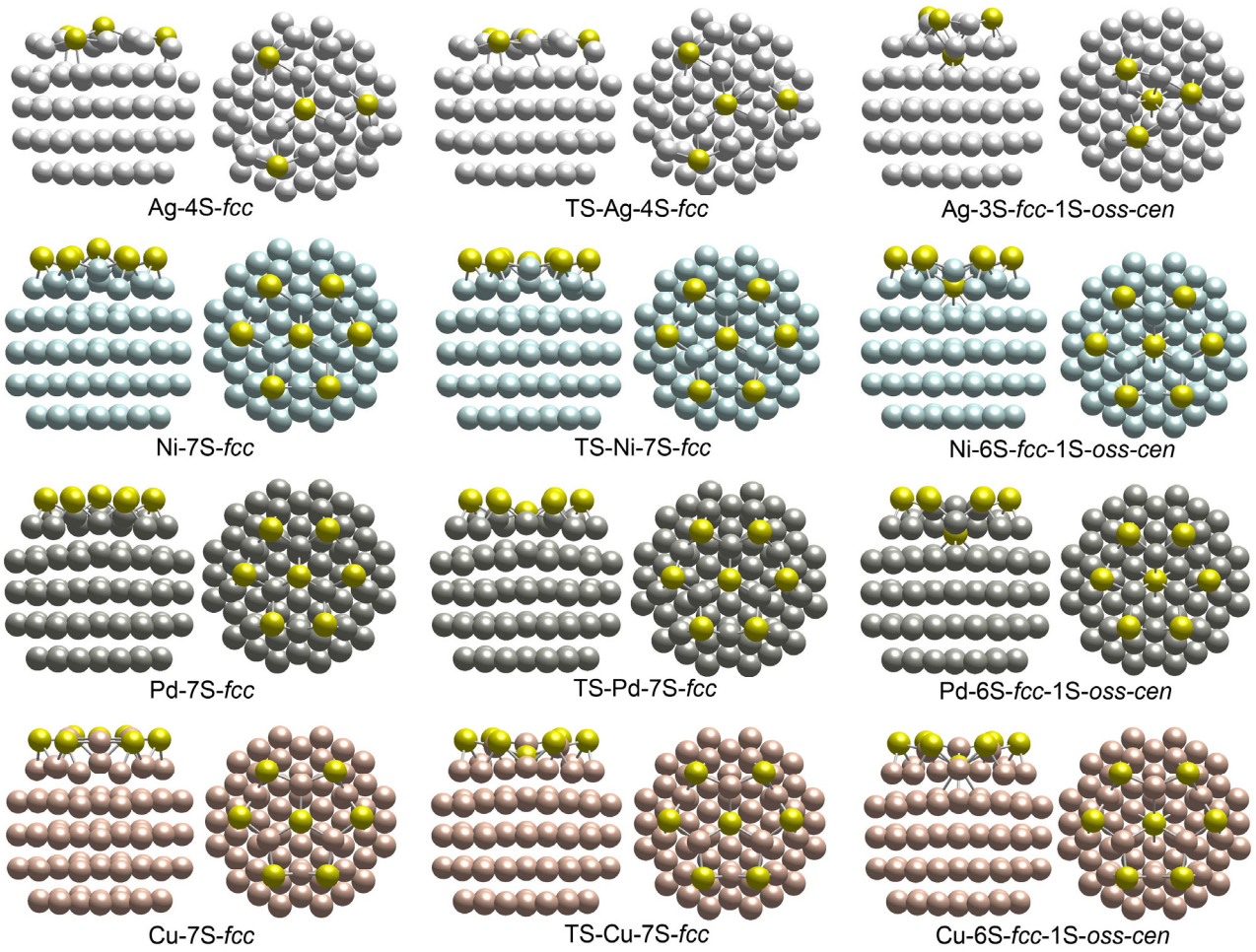


Figure 2. Side and top views of the initial (**left column**), transition (**central column**) and final (**right column**) states for diffusion of sulfur. Color coding: Ag—light gray; Ni—light blue; Pd—gray; Cu—orange and S—yellow.

Table 2. Bader charges (|e|) of sulfur in positions *fcc-cen* and *oss-cen*, and of the metal centers to which it is bound.

M_{79}	S (*fcc-cen*)	S (*oss-cen*)	M (*fcc-cen*)	M (*oss-cen*)
Rh_{79}	−0.23	−0.12	0.06; 0.09; 0.10	0.00; 0.00; 0.00; 0.08; 0.08; 0.10
Ir_{79}	−0.19	−0.02	0.07; 0.11; 0.12	−0.02; −0.02; −0.02; 0.05; 0.10; 0.12
Ni_{79}	−0.44	−0.44	0.10; 0.11; 0.12	0.06; 0.07; 0.07; 0.08; 0.08; 0.11
Pd_{79}	−0.15	−0.02	0.07; 0.08; 0.08	0.04; 0.05; 0.05; 0.09; 0.09; 0.12
Pt_{79}	−0.02	0.13	0.05; 0.05; 0.06	−0.01; 0.00; 0.00; 0.13; 0.13; 0.13
Cu_{79}	−0.60	–	0.16; 0.17; 0.18	–
Ag_{79}	−0.57	−0.57	0.13; 0.14; 0.14	0.07; 0.11; 0.11; 0.11; 0.11; 0.11
Au_{79}	–0.20	–	0.07; 0.08; 0.08	–

The density of states (DOS) difference plots for the d states of the metal centers bound to sulfur at *fcc-cen* position show that sulfur adsorption leads to a pronounced depletion of DOS in the range of −2.0 eV to 0.5 eV (around the Fermi level) and an increase in DOS below the Fermi level, 7.0 eV ÷ −2.0 eV (see Figure S1A,B in Supplementary Materials). Also, for all metal NPs, some additional states appear in the region −12 ÷ −16.5 eV (Figure S1C in Supplementary Materials).

We also calculated the d-band centers for the metal atoms from the *fcc-cen* site of M_{79} nanoparticles before and after S adsorption. In all the cases, a shift in the *d*-states to lower energies is observed after S adsorption (see Table 3), as for most of the metals, it is ~0.2 eV. In the case of Ag and Au NPs, where the *d*-band centers are very low in energy, −3.91 and −2.89 eV, respectively, this shift is negligible, which is one more indication of the weak interaction between the adsorbate and the corresponding nanoparticles. Small down shift in the d-band center upon S adsorption is also observed for S adsorption on M_{13} clusters [31].

Table 3. Values of the d-band center (ε_d, eV) of the metal atoms at the *fcc-cen* site before and after the adsorption of S.

M_{79}	ε_d (Pristine M_{79})	ε_d (S/M_{79})	Shift
Rh_{79}	−1.93	−2.09	−0.16
Ir_{79}	−2.55	−2.73	−0.18
Ni_{79}	−1.31	−1.45	−0.14
Pd_{79}	−1.51	−2.15	−0.64
Pt_{79}	−2.03	−2.27	−0.24
Cu_{79}	−2.27	−2.51	−0.24
Ag_{79}	−3.91	−3.99	−0.08
Au_{79}	−2.89	−2.91	−0.02

The charge density difference plots for the models with sulfur adsorbed at the *fcc-cen* site reveal a depletion of electron density from the metal centers adjacent to sulfur (blue regions), accompanied by a redistribution of electron density around these centers (see Figure 3). For Cu and Ag, where the Bader charge of S is most negative (−0.6 |e|), more significant electron accumulation (green regions) is observed at the S species compared to the other NPs.

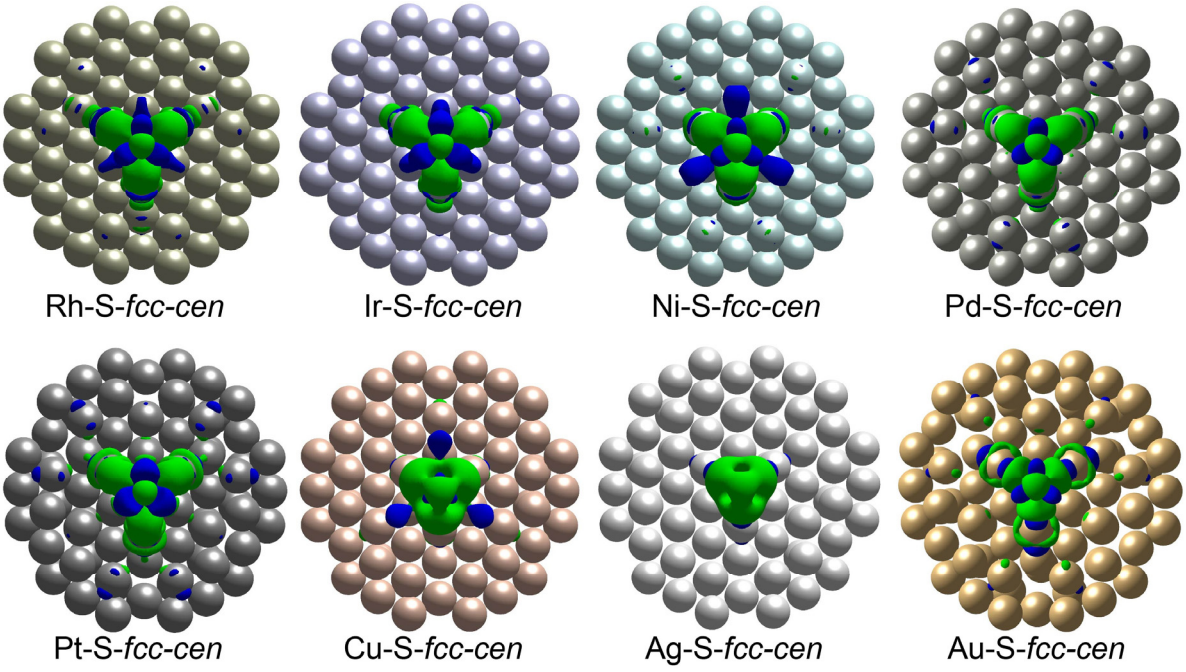


Figure 3. Top view of the charge density difference plots for the models with S adsorbed at the *fcc-cen* site on the M_{79} NPs. Green areas show an increase in electron density due to S addition, while blue areas indicate electron density depletion. The value for the 3D surface representing a constant value of the charge density (isosurface value) is 0.002 e/bohr^3.

3. Discussion

3.1. General Trends

The analysis of the stability of the S adsorption sites on the M_{79} nanoparticles shows several trends. For the metals of group 9 (Rh and Ir), the *hcp-cor* and *fcc-cor* sites are the most favorable ones; for group 10 (Ni, Pd, Pt)—*fcc-cen* and *fcc-cor*; and for group 11 (Cu, Ag and Au)—*fcc-cor*. The overall trend of the binding energy of sulfur located in the surface hollow positions is: Rh (−533 ÷ −517 kJ/mol) ~ Ir(−529 ÷ −497 kJ/mol) > Pt (−516 ÷ −493 kJ/mol) > Ni (−502 ÷ −487 kJ/mol) > Pd (−487 ÷ −473 kJ/mol) > Cu (−450 ÷ −410 kJ/mol) > Ag (−370 ÷ −354 kJ/mol) ~ Au (−386 ÷ −363 kJ/mol).

The occupation of the *d*-orbitals appears to be a key factor for determining the sulfur binding strength, since it correlates well with the BE of sulfur at the different hollow adsorption positions (see Figure 4 and Figure S2 in Supplementary Materials). Since sulfur possesses six valence electrons (two single electrons and two lone pairs), it prefers to interact with metal centers, which provide empty frontier orbitals. Thus, it is not surprising that it binds more strongly to *fcc* metals with lower occupation of the *d*-states, such as Rh and Ir, and less strongly to metals with completely filled d levels, such as Ag and Au. There is also a correlation between the *d*-band center of the studied metals and the BE of S (see Figure 4). As expected, the transition metals with higher energy of the *d*-band centers are more reactive towards S adsorption. In addition, the overall trend in the d-band center values of the metal atoms before S adsorption follows the order *hcp-cor* > *fcc-cor* > *hcp-edg* > *fcc-cen* (see Table S4 in Supplementary Materials), reflecting the higher reactivity of metal atoms with lower coordination numbers—those located on the edges and corners of the NPs (atoms at *cor* and edg sites)—compared to those with higher coordination numbers (located at the center of the (111) facet, *cen* sites).

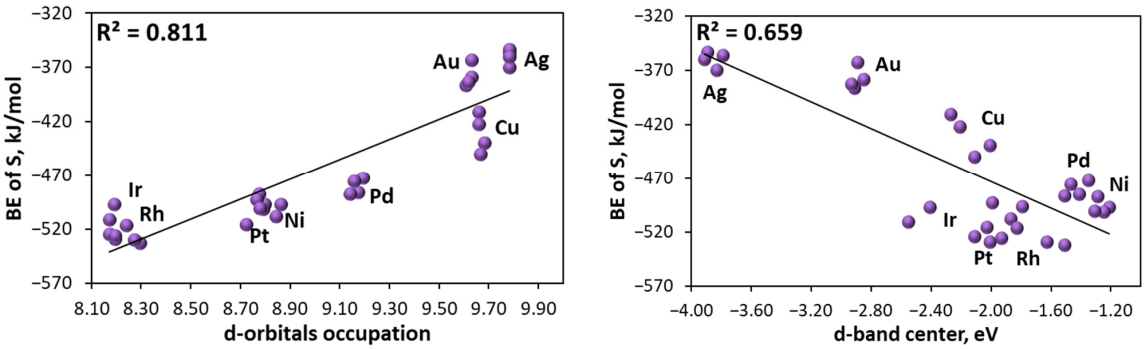


Figure 4. Correlation between the BE of the sulfur atom at the different hollow positions, the occupation of d-orbitals with electron density, and the *d*-band center of the metal atoms located at those positions before S adsorption.

As expected, the increase in the electron density of the adsorbed sulfur, i.e., its partial negative Bader charge, seems to be related to the electronegativity of the different metals (see Figure 5). The sulfur charge is most negative, −0.44, −0.60 and −0.57 |e|, when interacting with Ni, Cu and Ag metals, respectively, which have the lowest electronegativity (~1.9) among the *fcc* metals.

While previous studies focused on extended surfaces and considered only surface diffusion of sulfur [14,15], in our work we studied the diffusion of sulfur from the surface to the subsurface region, as the NP moiety possesses higher flexibility. Indeed, we found that, upon higher sulfur content—seven S per (111) facet, i.e., 58% or $^{7}/_{12}$ of a ML S coverage, such a process is exothermic for Ni, Pd and Ag NPs and mildly endothermic for the Cu NP. The relaxation energy partially accounts for the observed stability trend of structures with high sulfur concentration (see Figure 6). On the other hand, the relaxation energy

poorly correlates with the binding energy of sulfur at the *fcc-cen*/*oss-cen* sites (R^2 = 0.141, see Figure S3 in Supplementary Materials). However, the interaction energy explains the observed trend of the binding energy to a greater extent, since it shows a stronger correlation with the sulfur binding energy.

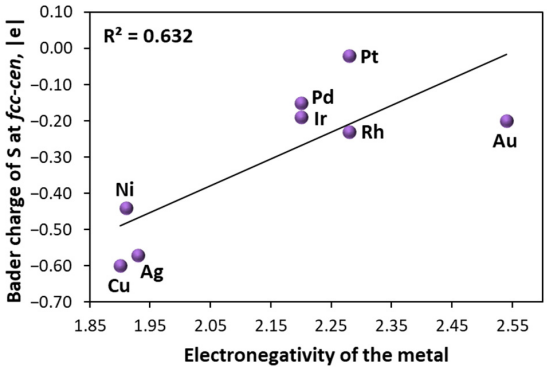


Figure 5. Correlation between the electronegativity of the metals and the Bader charge of S adsorbed at *fcc-cen* position. The electronegativity values are taken from ref. [32].

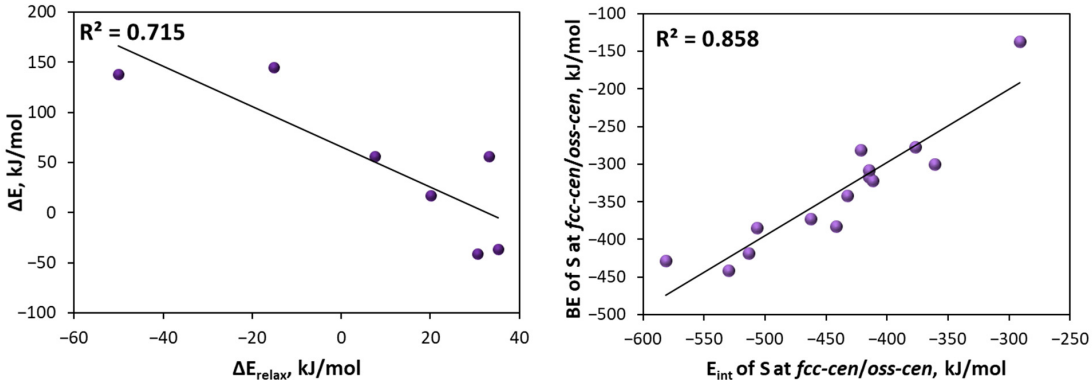


Figure 6. Correlations between: the difference in the relaxation energies in each series, ΔE_{relax}, and the relative energies, ΔE, of the structures with seven sulfur atoms (**left panel**), and sulfur binding energy at *fcc-cen*/*oss-cen* sites in models with seven S atoms and the interaction energy, E_{int}, of S at the same sites (**right panel**). In both graphs, Ag is excluded, since in the structure with seven S species adsorbed on the surface, the S atom at the *fcc-cen* position migrates spontaneously to the subsurface layer of the NP (*oss-cen* site).

3.2. Nanoparticles Versus Surfaces

Rodríguez et al. [14] modeled the adsorption and surface diffusion of sulfur on the (111), (100), (110), and (211) surfaces of the *fcc* metals using RPBE functional and 550 eV cutoff. Since in the current research the adsorption to (111) facets of the M_{79} NPs were studied, we compared the BE of S species located at the *fcc-cen* adsorption site. To ensure a more accurate comparison of both sets of data, we recalculated the BE values for our models at the *fcc* site on the (111) facets, employing the RPBE functional and a 550 eV cutoff (Table 4). In this case, the comparison between NPs and extended surfaces shows that, essentially for all TM systems, the absolute BE values are higher for the NP models, which can be rationalized by their greater flexibility. For Ir, Ni, Pd and Cu, the differences in the BE values are within 5–9 kJ/mol. Larger differences are found for Rh and Ag, 14 and 19 kJ/mol, respectively, while for the most flexible Pt and Au, S binds more strongly compared to the corresponding (111) surfaces by 31 and 40 kJ/mol, respectively. Nevertheless, the order of interaction strength of S species with both models (NPs and extended surfaces) remains the same: Rh > Pt > Ir > Ni > Pd > Cu > Au > Ag. The results also show that increasing the energy cutoff has minor effect on the BE values, as the values

obtained with 415 and 550 eV agree within 1 kJ/mol for both investigated functionals (see Tables S5 and S6 in Supplementary Materials). We also calculated both contributions to the BE values namely, interaction energy and relaxation energy of the metal nanoparticle. The highest relaxation energies were calculated for Au and Pt, 73 and 64 kJ/mol, respectively, while lower values of 16–27 kJ/mol were obtained for the other *fcc* metals.

Table 4. Comparison of the binding energies of S adsorbed at *fcc-cen* site on M_{79} NPs with literature data for BE values at *fcc* site on (111) transition metal surfaces. All the values are in kJ/mol.

M_{79} NP S (*fcc-cen Site*) This Work PBE/415 eV		**M_{79} NP S (*fcc-cen Site*) This Work RPBE/550 eV**	**M(111) Surface S (*fcc Site*) Ref [14] RPBE/550 eV**		**ΔBE [a] PBE—RPBE**	**ΔBE [a] RPBE—RPBE**
Rh_{79}	−526	−487	Rh(111)	−473/−478 [15]	−53	−14
Ir_{79}	−511	−472	Ir(111)	−466	−45	−6
Ni_{79}	−501	−458	Ni(111)	−453	−48	−5
Pd_{79}	−487	−448	Pd(111)	−438	−49	−9
Pt_{79}	−516	−477	Pt(111)	−447	−69	−31
Cu_{79}	−411	−380	Cu(111)	−385	−26	5
Ag_{79}	−360	−333	Ag(111)	−314	−46	−19
Au_{79}	−363	−343	Au(111)	−304	−59	−40

[a] Energy difference BE(M_{79})–BE(M(111)).

On the extended (111) surfaces, there are only two types of hollow coordination sites, fcc and hcp. Our nanoparticle model provides greater variety of adsorption positions, as sulfur may occupy positions close to the edges and corners of the (111) facets. On the surface (111) models, sulfur prefers to bind to the *fcc* sites, while our results show that on NPs, in some cases, the closest equivalent of the *fcc* sites, the *fcc-cen* position, is not the most favorable one. As it was already summarized, on the metals of groups 9 (Rh and Ir) and 11 (Cu, Ag and Au), sulfur prefers to bind close to the corners and edges of the NPs (*hcp-cor* and *fcc-cor* sites for group 9 and *fcc-cor* for group 11). However, one should have in mind that the type of metal also matters. For example, the *fcc-cen* position in the case of Rh_{79} and Ag_{79} NPs is disfavored by only 7 and 10 kJ/mol, respectively, compared to the corresponding most stable sites, while on Cu_{79} NP, the difference is significant and *fcc-cen* is less stable by 40 kJ/mol.

Rodríguez et al. [14] also calculated the Bader charge of the adsorbed sulfur species on the M(111) models. Their obtained values for S adsorption on the *fcc* position are very close to ours for the *fcc-cen* position of the modeled M_{79} NPs (Table 5). The differences are within 0.01–0.06 |e|. Our calculated value for the S/Au_{79} structure, −0.20 |e|, is also in line with the reported Bader charge by Carro et al. for the adsorption of S on Au(111) surface [25].

Table 5. Comparison of the Bader charges (|e|) of sulfur at *fcc-cen* position on the studied NPs and in *fcc* position on (111) surfaces [14].

M_{79} NP S (*fcc-cen Site*) This Work		**M(111) Surface S (*fcc Site*) Ref [14]**		**Δ [a]**
Rh_{79}	−0.23	Rh(111)	−0.24	0.01
Ir_{79}	−0.19	Ir(111)	−0.24	0.05
Ni_{79}	−0.44	Ni(111)	−0.47	0.03
Pd_{79}	−0.15	Pd(111)	−0.18	0.03
Pt_{79}	−0.02	Pt(111)	−0.08	0.06
Cu_{79}	−0.60	Cu(111)	−0.56	−0.04
Ag_{79}	−0.57	Ag(111)	−0.52	−0.05
Au_{79}	−0.20	Au(111)	−0.24	0.04

[a] Difference in the Bader charge values of S species positioned, respectively, at *fcc-cen* and *fcc* sites of M_{79} and M(111) models.

4. Computational Details

The DFT calculations were performed under periodic boundary conditions using Vienna ab initio simulation package (VASP) [33,34], version 5.4.4. Consistent with our previous research on metal NPs, geometry optimizations were carried out using the Perdew–Burke–Ernzerhof (PBE) exchange-correlation functional [35], which provides a reliable and accurate description of TM bulks and surfaces and adsorptions upon [36–39] and a plane wave basis set with a 415 eV cutoff for the kinetic energy was used, enough to deliver results with chemical precision below 0.04 eV. The interactions between core and valence electrons were described by the core projector augmented wave (PAW) method [40]. The Brillouin zone was sampled using only the Γ point, and orbital occupancies were determined using the Methfessel–Paxton method with a smearing width of 0.2 eV [41]. Geometry optimizations were continued until all forces on the atoms became less than 0.02 eV/Å, and the electronic convergence threshold was set to 1×10^{-6} eV. Dispersion corrections were not included in our study. Our test calculations on the structures with S species located at *fcc-cen* and *oss-cen* positions on all *fcc* transition metal NPs using the Grimme D3 dispersion correction (Table S7 in Supplementary Materials) showed that the absolute values of BE are increased by 16 to 38 kJ/mol. This systematic shift in the BE values does not change the main conclusions of our study.

All calculations were performed in a non-spin-polarized (closed-shell) framework, except for systems containing Ni, which were treated with spin polarization. The nanoparticle models consist of 79 atoms arranged in a truncated octahedral shape exhibiting eight (111) facets (each composed of 12 atoms), and six small (100) facets (composed of only 4 atoms). The NPs were placed in a cubic box with a size of $20 \times 20 \times 20$ Å^3, providing a minimum distance of 10 Å between the periodic images to prevent interactions between the atoms from the different images. For correct description of the orbital occupancy (triplet state) of the isolated S atom, an asymmetric box of $9 \times 10 \times 11$ Å^3 was used.

The binding energy (BE, or adsorption energy) per S atom is calculated in the following way:

$$BE = [E(S_n/M_{79}) - E(M_{79}) - n \times E(S)]/n \quad (1)$$

where n is the number of the sulfur atoms (1, 4, or 7), $E(M_{79})$ is the energy of the corresponding metal nanoparticle (M = Rh, Ir, Ni, Pd, Pt, Cu, Ag, and Au), $E(S_n/M_{79})$ is the energy of the metal nanoparticle with the corresponding number of sorbed sulfur atom(s), and E(S) is the energy of the sulfur atom isolated in a gas phase. According to this definition, negative BE values indicate an energetically favorable interaction between the nanoparticle and sulfur, i.e., energy is released during sulfur sorption.

The relative energy, ΔE, shown in Figure 6, is defined as:

$$\Delta E = E(\text{M-6S-}\textit{fcc}\text{-1S-}\textit{oss}) - E(\text{M-7S-}\textit{fcc}) \quad (2)$$

and, i.e., it represents the stabilization of S atom located at the center octahedral position (*oss-cen*) with respect to the *fcc-cen* surface adsorption. The difference in the relaxation energy, ΔE_{relax}, shown in Figure 6, is calculated as the energy obtained by single-point calculation of the models S_7/M_{79} with S removed at the *fcc-cen/oss-cen* position minus the energy of the optimized structure S_7/M_{79} with S removed at the *fcc-cen* position.

The interaction energy, E_{int}, shown in Figure 6, is calculated using the following expression:

$$E_{int} = E(S_7/M_{79}) - E(S_6/M_{79}) - E(S) \quad (3)$$

where $E(S_7/M_{79})$ is the energy of the metal nanoparticle with seven sorbed sulfur atom(s); $E(S_6/M_{79})$ is the single point energy of the structure S_7/M_{79} with S removed at the *fcc-cen* position; and E(S) is the energy of the sulfur atom isolated in a gas phase.

The transition states (TSs) for S subsurface migration were obtained using the DIMER method [42]. The obtained TS structures were confirmed by the presence of an imaginary frequency along the direction of the diffusion of the sulfur atom from the surface to the subsurface region, i.e., *fcc-cen* → *oss-cen*. The charge density difference, as well as all models, were visualized with the VESTA program [43].

5. Conclusions

The interaction of sulfur with M_{79} nanoparticles of all *fcc* metals—Rh, Ir, Ni, Pd, Pt, Cu, Ag, Au—was computationally studied by DFT means. It was found that, when one sulfur atom interacts with the nanoparticles, it strongly prefers to adsorb on the surface. Upon higher sulfur coverage (58% or $^7/_{12}$ of a ML), the subsurface diffusion of sulfur becomes energetically favorable for Ni, Pd, and Ag nanoparticles, and slightly endothermic for Cu, accompanied by low activation barriers. Among the studied metals, sulfur exhibits the strongest binding to Rh and Ir, and the weakest binding to Ag and Au. The binding strength is mainly driven by the occupation of d-orbitals. However, the d-band center—a common descriptor for reactivity—also, to some extent, predicts the observed trend in the binding energies of S. The calculated electronic characteristics reveal a partial charge transfer from the metal centers to the adsorbed sulfur species, resulting in a partial positive charge of these metal centers, which is expected to modify their chemical and catalytic properties. In addition, the adsorption of sulfur leads to stabilization of their d-states (i.e., a shift in the d-states to lower energies).

Supplementary Materials: The following supporting information can be downloaded at: https://www.mdpi.com/article/10.3390/catal16050408/s1, Figure S1: Density of states (DOS) difference plots for the d states of the metal centers bound to S species in S/M_{79} systems with respect to the corresponding M_{79} systems; Figure S2: Correlation between the BE of the sulfur atom at the different hollow positions (hcp-cor, fcc-cor, hcp-edg, and fcc-cen) and the d-band center/occupation of the d-orbitals of the metal atoms located at those positions before S adsorption; Figure S3: Correlation between the relaxation energy, ΔErelax, and the binding energy of S at fcc-cen/oss-cen sites, BE, of the structures with seven sulfur atoms; Table S1. Relative energies, ΔE in kJ/mol with respect to the most energetically stable structure in the series, BE, binding energy of the sulfur atom, BE in kJ/mol, and M-S bond lengths in pm for the models with one S ad/absorbed on Rh_{79} and Ir_{79} NPs; Table S2. Relative energies, ΔE in kJ/mol with respect to the most energetically stable structure in the series, BE, binding energy of the sulfur atom, BE in kJ/mol, and M-S bond lengths in pm for the models with one S ad/absorbed on Ni_{79}, Pd_{79} and Pt_{79} NPs; Table S3. Relative energies, ΔE in kJ/mol with respect to the most energetically stable structure in the series, BE, binding energy of the sulfur atom, BE in kJ/mol, and M-S bond lengths in pm for the models with one S ad/absorbed on Cu_{79}, Ag_{79} and Au_{79} NPs; Table S4. Values of the d-band center (εd,eV) of the metal centers located at the surface sites before S adsorption; Table S5. Comparison of the binding energies (BE, kJ/mol) of the sulfur species interacting with M_{79} nanoparticles obtained using the PBE functional with 415 and 550 eV cutoff energies; Table S6. Comparison of the binding energies (BE, kJ/mol) of the sulfur species interacting with M_{79} nanoparticles obtained using the RPBE functional with 415 and 550 eV cutoff energies; Table S7. Comparison of the binding energies (BE, kJ/mol) of the sulfur species interacting with M_{79} nanoparticles, calculated with and without dispersion correction (PBE and PBE-D3, respectively); Geometrical coordinates of the optimized structures in CONTCAR file format.

Author Contributions: Conceptualization, H.A.A. and F.V.; Methodology, I.Z.K. and H.A.A.; Software, H.A.A.; Formal analysis, I.Z.K. and H.A.A.; Investigation, I.H., P.V.K. and I.Z.K.; Writing—original draft preparation, B.S. and I.Z.K.; Writing—review and editing, H.A.A. and F.V.; Visualization, I.Z.K.; Supervision, H.A.A. and I.Z.K.; Project administration, H.A.A.; Funding acquisition, H.A.A. All authors have read and agreed to the published version of the manuscript.

Funding: This research was funded by European Union-NextGenerationEU, through the National Recovery and Resilience Plan of the Republic of Bulgaria, project No BG-RRP-2.004-0008.

Data Availability Statement: The original contributions presented in this study are included in the article/Supplementary Material. Further inquiries can be directed to the corresponding authors.

Acknowledgments: I.Z.K., I.H., P.V.K., and B.S. are grateful to the European Union-NextGenerationEU, through the National Recovery and Resilience Plan of the Republic of Bulgaria, project No BG-RRP-2.004-0008 for the financial support. H.A.A. gratefully acknowledges the support provided by the project UNITe BG16RFPR002-1.014-0004 funded by PRIDST. Computational resources at Discoverer supercomputer have been provided by Discoverer PetaSC and EuroHPC JU. The research has been supported by the Spanish Ministry of Science, Innovation and Universities (MICIUN) MCIN/AEI/10.13039/501100011033 PID2021-126076NB-I00 and PID2024-159906NB-I00 projects, funded partially by FEDER Una manera de hacer Europa, and Unidad de Excelencia María de Maeztu CEX2021-001202-M grants, including funding from European Union, and the Generalitat de Catalunya grant 2021SGR00079. F.V. thanks the ICREA Academia Award 2023 Ref. Ac2216561.

Conflicts of Interest: The authors declare no conflicts of interest.

References

1. Bartholomew, C.H. Mechanisms of catalyst deactivation. *Appl. Catal. A* **2001**, *212*, 17–60. [CrossRef]
2. Laosiripojana, N.; Rajesh, S.K.; Singhto, W.; Palikanon, T.; Pengyong, S. Effects of H_2S, CO_2, and O_2 on Catalytic Methane Steam Reforming over Ni Catalysts Supported on CeO_2 and Al_2O_3. In Proceedings of the Joint International Conference on "Sustainable Energy and Environment (SEE), Hua Hin, Thailand, 1–3 December 2004; Available online: https://www.researchgate.net/publication/242700733_Effects_of_H2S_CO2_and_O2_on_Catalytic_Methane_Steam_Reforming_over_Ni_Catalyst_on_CeO2_and_Al2O3_Supports (accessed on 22 December 2025).
3. Lee, J.; Jang, E.J.; Oh, D.G.; Szanyi, J.; Kwak, J.H. Morphology and size of Pt on Al_2O_3: The role of specific metal-support interactions between Pt and Al_2O_3. *J. Catal.* **2020**, *385*, 204–212. [CrossRef]
4. Allian, A.D.; Takanabe, K.; Fujdala, K.L.; Hao, X.; Truex, T.J.; Cai, J.; Buda, C.; Neurock, M.; Iglesia, E. Chemisorption of CO and mechanism of CO oxidation on supported platinum nanoclusters. *J. Am. Chem. Soc.* **2011**, *133*, 4498–4517. [CrossRef] [PubMed]
5. van Spronsen, M.A.; Frenken, J.W.M.; Groot, I.M.N. Surface science under reaction conditions: CO oxidation on Pt and Pd model catalysts. *Chem. Soc. Rev.* **2017**, *46*, 4347–4374. [CrossRef]
6. Gracia, F.; Guerrero, S.; Wolf, E.; Miller, J.; Kropf, A. Kinetics, operando FTIR, and controlled atmosphere EXAFS study of the effect of sulfur on Pt-supported catalysts during CO oxidation. *J. Catal.* **2005**, *233*, 372–387. [CrossRef]
7. Mowery, D.L.; McCormick, R.L. Deactivation of alumina supported and unsupported PdO methane oxidation catalyst: The effect of water on sulfate poisoning. *Appl. Catal. B* **2001**, *34*, 287–297. [CrossRef]
8. Lampert, J.; Kazi, M.; Farrauto, R. Palladium catalyst performance for methane emissions abatement from lean burn natural gas vehicles. *Appl. Catal. B* **1997**, *14*, 211–223. [CrossRef]
9. Kim, H.; Kim, K.H.; Kim, J.; Kwak, J.H. Enhancing sulfur tolerance in Pt/TiO_2 catalysts: Effect of H_2O in CO oxidation. *Chem. Eng. J.* **2026**, *527*, 171876. [CrossRef]
10. Kim, J.Y.; Lindgren, P.; Zhang, Y.-J.; Kim, S.K.; Valentin, T.M.; Jung, H.-T.; Peterson, A.A. Sulfur promotes hydrogen evolution on molybdenum carbide catalysts. *Mater. Adv.* **2021**, *2*, 4867–4875. [CrossRef]
11. Feng, S.; Mu, J.; Lin, X.; Song, X.; Liu, S.; Shi, W.; Zhang, W.; Wu, G.; Jiayue, Y.; Dong, W.; et al. Sulfur-poisoning on Rh NP but sulfur-promotion on single-Rh1-site for methanol carbonylation. *Appl. Catal. B Environ.* **2023**, *325*, 122318. [CrossRef]
12. Daga, Y.; Kizilkaya, A.C. Mechanistic insights into the effect of sulfur on the selectivity of cobalt-catalyzed Fischer–Tropsch synthesis: A DFT study. *Catalysts* **2022**, *12*, 425. [CrossRef]
13. Li, Y.; Wu, H.R.; Yu, Y.; Chen, M.Y.; Zhao, K.M.; Li, W.D.; Rong, S.Y.; Xue, D.P.; Zhang, J.N.; Lu, B.A. High-shell sulfur doping enhances Mn–N4 spin states and boosts oxygen reduction reaction performance in both acidic and alkaline media. *Small* **2025**, *21*, e2411678. [CrossRef] [PubMed]

14. Larghi, C.; Porta, A.; Etzi, M.; Fiori, G.; Visconti, C.G.; Szanyi, J.; Lietti, L. Reactivity and Characterization of S-Poisoning on Ru/Al_2O_3 Catalysts for CO_2 Methanation. *Appl. Catal. B Environ. Energy* **2026**, *385*, 126336. [CrossRef]
15. Bernard Rodríguez, C.R.; Santana, J.A. Adsorption and diffusion of sulfur on the (111), (100), (110), and (211) surfaces of FCC metals: Density functional theory calculations. *J. Chem. Phys.* **2018**, *149*, 204701. [CrossRef]
16. Mavrikakis, M.; Rempel, J.; Greeley, J.P.; Hansen, L.B.; Nørskov, J.K. Atomic and molecular adsorption on Rh(111). *J. Chem. Phys.* **2002**, *117*, 6737–6744. [CrossRef]
17. Kibria, M.G.; Shattique, M.R. The $(\sqrt{3} \times \sqrt{3})R30^\circ$ sulfur overlayer on the Ir(111) surface: A DFT study. In Proceedings of the 9th International Forum on Strategic Technology (IFOST), Cox's Bazar, Bangladesh, 21–23 October 2014; pp. 460–463. [CrossRef]
18. Nilekar, A.U.; Greeley, J.; Mavrikakis, M. A Simple Rule of Thumb for Diffusion on Transition-Metal Surfaces. *Angew. Chem. Int. Ed.* **2006**, *45*, 7046–7049. [CrossRef]
19. Galea, N.M.; Lo, J.M.H.; Ziegler, T. A DFT study on the removal of adsorbed sulfur from a nickel(111) surface: Reducing anode poisoning. *J. Catal.* **2009**, *263*, 380–389. [CrossRef]
20. Das, N.K.; Saidi, W.A. Effects of Cr-doping on the adsorption and dissociation of S, SO, and SO_2 on Ni(111) surfaces. *J. Chem. Phys.* **2017**, *146*, 154701. [CrossRef]
21. Alfonso, D.R.; Cugini, A.V.; Sholl, D.S. Density functional theory studies of sulfur binding on Pd, Cu and Ag and their alloys. *Surf. Sci.* **2003**, *546*, 12–26. [CrossRef]
22. Ungerer, M.J.; van Sittert, C.G.C.E.; de Leeuw, N.H. Behavior of S, SO, and SO_3 on Pt(001), (011), and (111) surfaces: A DFT study. *J. Chem. Phys.* **2021**, *154*, 194701. [CrossRef]
23. Liu, D.-J.; Walen, H.; Oh, J.; Lim, H.; Evans, J.W.; Kim, Y.; Thiel, P.A. Search for the structure of a sulfur-induced reconstruction on Cu(111). *J. Phys. Chem. C* **2014**, *118*, 29218–29223. [CrossRef]
24. Xu, L.; Lin, J.; Bai, Y.; Mavrikakis, M. Atomic and molecular adsorption on Cu(111). *Top. Catal.* **2018**, *61*, 7–8. [CrossRef]
25. Alvarez Soria, L.; Zampieri, G.; Martiarena, M.L. Sulfur-induced reconstruction of Ag(111) surfaces studied by DFT. *J. Phys. Chem. C* **2011**, *115*, 9587–9592. [CrossRef]
26. Carro, P.; Andreasen, G.; Vericat, C.; Vela, M.E.; Salvarezza, R.C. New aspects of the surface chemistry of sulfur on Au(111): Surface structures formed by gold–sulfur complexes. *Appl. Surf. Sci.* **2019**, *487*, 848–856. [CrossRef]
27. Daigle, A.D.; BelBruno, J.J. Density Functional Theory Study of the Adsorption of Nitrogen and Sulfur Atoms on Gold (111), (100), and (211) Surfaces. *J. Phys. Chem. C* **2011**, *115*, 22987. [CrossRef]
28. Huang, W.; Lai, W.; Xie, D. A DFT investigation of sulfur adsorption on Ir(100). *J. Theor. Comput. Chem.* **2007**, *6*, 177–185. [CrossRef]
29. Ruvireta, J.; Vega, L.; Viñes, F. Cohesion and coordination effects on transition metal surface energies. *Surf. Sci.* **2017**, *664*, 45–49. [CrossRef]
30. Viñes, F.; Illas, F.; Neyman, K.M. Density Functional Calculations of Pd Nanoparticles Using a Plane-Wave Method. *J. Phys. Chem. A* **2008**, *112*, 8911–8915. [CrossRef]
31. Monteiro, R.F.; Palheta, J.M.T.; Grison, T.G.; Filho, O.R.; Parreira, R.L.T.; Guedes-Sobrinho, D.; Rêgo, C.R.C.; Dias, A.C.; de Araújo Batista, K.E.; Piotrowski, M.J. Interpretable, Physics-Informed Learning Reveals Sulfur Adsorption and Poisoning Mechanisms in 13-Atom Icosahedra Nanoclusters. *arXiv* **2026**, arXiv:2601.13845.
32. Allred, A.L. Electronegativity values from thermochemical data. *J. Inorg. Nucl. Chem.* **1961**, *17*, 215. [CrossRef]
33. Kresse, G.; Furthmüller, J. Efficient Iterative Schemes for Ab Initio Total-Energy Calculations Using a Plane-Wave Basis Set. *Phys. Rev. B* **1996**, *54*, 11169. [CrossRef] [PubMed]
34. Kresse, G.; Furthmüller, J. Efficiency of Ab-Initio Total Energy Calculations for Metals and Semiconductors Using a Plane-Wave Basis Set. *Comput. Mater. Sci.* **1996**, *6*, 15–50. [CrossRef]
35. Perdew, J.P.; Burke, K.; Ernzerhof, M. Generalized gradient approximation made simple. *Phys. Rev. Lett.* **1996**, *77*, 3865–3868. [CrossRef] [PubMed]
36. Vega, L.; Ruvireta, J.; Viñes, F.; Illas, F. Performance of exchange–correlation functionals for the adsorption of molecules on metal surfaces. *J. Chem. Theory Comput.* **2018**, *14*, 395–403. [CrossRef]
37. Janthon, P.; Viñes, F.; Sirijaraensre, J.; Limtrakul, J.; Illas, F. Assessing the accuracy of DFT methods for describing adsorption on metal surfaces. *Catal. Sci. Technol.* **2017**, *7*, 807–816. [CrossRef]
38. Piqué, O.; Koleva, I.Z.; Viñes, F.; Aleksandrov, H.A.; Vayssilov, G.N.; Illas, F. Subsurface Carbon: A General Feature of Noble Metals. *Angew. Chem. Int. Ed.* **2019**, *58*, 1744–1748. [CrossRef]
39. Vega, L.; Viñes, F. Generalized gradient approximation adjusted to transition metals properties: Key roles of exchange and local spin density. *J. Comput. Chem.* **2020**, *41*, 2598–2603. [CrossRef]
40. Blöchl, P.E. Project augmented-wave method. *Phys. Rev. B* **1994**, *50*, 17953. [CrossRef]
41. Methfessel, M.; Paxton, A.T. High-precision sampling for Brillouin-zone integration in metals. *Phys. Rev. B Condens. Matter Mater. Phys.* **1989**, *40*, 3616–3621. [CrossRef]

42. Henkelman, G.; Jónsson, H. A dimer method for finding saddle points on high dimensional potential surfaces using only first derivatives. *J. Chem. Phys.* **1999**, *111*, 7010. [CrossRef]
43. Momma, K.; Izumi, F. VESTA 3 for three-dimensional visualization of crystal, volumetric and morphology data. *J. Appl. Crystallogr.* **2011**, *44*, 1272–1276. [CrossRef]

Disclaimer/Publisher's Note: The statements, opinions and data contained in all publications are solely those of the individual author(s) and contributor(s) and not of MDPI and/or the editor(s). MDPI and/or the editor(s) disclaim responsibility for any injury to people or property resulting from any ideas, methods, instructions or products referred to in the content.